

Deep learning–based intelligent measurement methods and system for CMM

Zhen-Ying Cheng, Yuan Sun, Kang Hu, Jie Li, Tien-Fu Lu, and
Rui-Jun Li

Abstract

Extensive manual intervention and management are typically required when using coordinate measuring machines (CMMs) for inspections in production lines leading to low efficiency. This study presents a deep learning–based intelligent measurement method and system for measuring typical features (including holes, cylinders, balls, steps, and slots) of common components to improve inspection efficiency. This method combines vision sensors and a trigger probe. The You Only Look Once algorithm was employed to learn and achieve intelligent detection of features. An image-matching algorithm based on image inverse perspective transformation was designed, and the ant colony algorithm was implemented to optimize the measurement sequence. Then, an automatic approach for feature measurement path planning was designed. The presented system was tested using CMM, and a component with multiple typical features was measured. Results show that this method and system can be efficaciously implemented for intelligent measurement of typical features.

Index Terms: CMM, Intelligent measurement, Cooperative sensor configuration

ACKNOWLEDGEMENTS

This research was partly funded by the National Natural Science Foundation of China (52175506, 52075143).

Corresponding author: Rui-Jun Li (e-mail: rj-li@hfut.edu.cn).

Zhen-Ying Cheng, Yuan Sun, Kang Hu, Jie Li and Rui-Jun Li are with the School of Instrument Science and Opto–Electronics Engineering, Hefei University of Technology, Hefei 230009, China(e-mail: rj-li@hfut.edu.cn). Tien-Fu Lu is with the School of Mechanical Engineering, University of Adelaide, SA 5005, Australia(e-mail: tien-fu.lu@adelaide.edu.au).

Deep learning–based intelligent measurement methods and system for CMM

Abstract

Extensive manual intervention and management are typically required when using coordinate measuring machines (CMMs) for inspections in production lines leading to low efficiency. This study presents a deep learning–based intelligent measurement method and system for measuring typical features (including holes, cylinders, balls, steps, and slots) of common components to improve inspection efficiency. This method combines vision sensors and a trigger probe. The You Only Look Once algorithm was employed to learn and achieve intelligent detection of features. An image-matching algorithm based on image inverse perspective transformation was designed, and the ant colony algorithm was implemented to optimize the measurement sequence. Then, an automatic approach for feature measurement path planning was designed. The presented system was tested using CMM, and a component with multiple typical features was measured. Results show that this method and system can be efficaciously implemented for intelligent measurement of typical features.

Index Terms: CMM, Intelligent measurement, Cooperative sensor configuration

1. Introduction

The demands for high manufacturing accuracy of mechanical components have ever been increasing following the high-speed development of aerospace, electronics, automotive, and other manufacturing fields. Measuring these components' key features is an important part of manufacturing accuracy inspection. Coordinate measuring machines (CMMs) have become the most widely used measurement instruments owing to their high accuracy. However, the manually programmed measurement approach does not allow CMMs to be well integrated into automated production. Therefore, research on enabling CMMs to make intelligent decisions and minimize human intervention and management in the measurement process has become a pressing need.

Computer-aided process planning techniques have been popularly studied to guide the measurement of components by using computer-aided design (CAD) models. These

techniques include intelligent extraction of inspection information [1-3], sampling strategies, and planning of inspection paths [4]. These techniques did reduce the reliance on manual operations. However, the alignment of CAD models with the machine coordinate system of CMM still requires significant manual input, and accurate CAD models are not always available for all components. Therefore, some studies integrated multiple sensors on CMM to develop measurement methods that do not rely on CAD models, which are classified as complementary, competitive, and cooperative systems according to sensor configuration [5].

In complementary sensor configuration, sensors are not directly dependent on each other but can be combined to provide complete information about a component. Bradley et al. [6] proposed a complementary sensor measurement method combining a laser scanner and a trigger probe. The laser scanner provides the required dense three-dimensional (3D) points on a free-form surface, and the trigger probe accurately defines the boundaries of the patch. Zhao et al. [7] proposed a method to automatically generate inspection plans for CMMs by combining a trigger probe and a laser scanner. A knowledge-based sensor selection method was implemented to select a suitable sensor for each feature to be inspected. In addition, the developed inspection planning module automatically planned the measurement strategy. The complementary sensor systems described above yield complete component information. However, data from different sensors are simply unified in the same coordinate system as the final digitized result, leading to limited measurement accuracy [9].

A competitive sensor configuration means that each sensor measures the same feature independently to reduce measurement uncertainty and avoid erroneous measurements. Huang et al. [8] proposed a dynamic sensing modeling approach with a trigger probe and an area laser scanner. Components are first scanned using a laser scanner to capture their overall shape and then measured using a trigger probe. Finally, the surface model is incrementally updated using a Kalman filter to fuse the trigger probe data. Yu et al. [9] used an optical scanner to acquire coordinate data and then an intelligent feature recognition and segmentation algorithm to extract the overall surface information of the component to guide the trigger probe to re-measure each feature.

The measurement results were used to compensate for the scanned data. The above competitive sensor systems repeatedly measure the whole component several times and then update the results using data fusion. These competitive sensor systems improve the accuracy more than complementary sensor configuration, but repeated measurements make the system less efficient.

In cooperative sensor configuration, information interaction occurs between sensors, that is, the information obtained by one sensor is used to guide the measurements of another sensor. Lu et al. [10] proposed a multi-sensor approach that integrates contact scanning and point laser probes. The point laser probe acquires a priori path information, and the planned path is subsequently used to guide the contact scanning probe to quickly and accurately digitize complex surfaces. Our group [11] has proposed an automated deep hole measurement system that combines stereo vision and a trigger probe. The Zhang Zhengyou calibration method is used to calibrate the cameras, the stereo vision algorithm is used to determine the spatial location of the probe and the deep hole, and the trigger probe is guided to measure the deep hole using the location information. Once the camera position changes, the coefficients of the calibrated camera need to be used again, and the calibration process and coordinate system conversion operation are complicated. Then, a self-calibrating, high-precision vision method is proposed using a new optical structure that eliminates complex calibration steps [12]. This method can guide the probe tip into micro holes with diameters less than 100 μm . However, the overall intelligent measurement of the components has not yet been achieved.

This study proposes an intelligent measurement system for CMM by combining vision sensors and touch trigger probes to achieve intelligent measurement of typical features on components based on the group's previous research. The system has a cooperative sensor configuration, component images are captured by vision sensors, and information about features on components is extracted using a deep learning-based intelligent algorithm. Then, the path and sampling strategy for probe measurement are planned. The system is simple in structure, does not require CAD models and complex camera calibration, and obtains final results by triggering the probe with high

measurement accuracy without the inconvenience of data fusion and repeated measurements. This paper is further structured as follows: Section 2 introduces the design of the intelligent measurement system. Section 3 discusses the working principles of the intelligent method. Section 4 presents the experiments and analysis. Section 5 concludes the study.

2. Measurement system design

2.1 Configuration of the measurement system

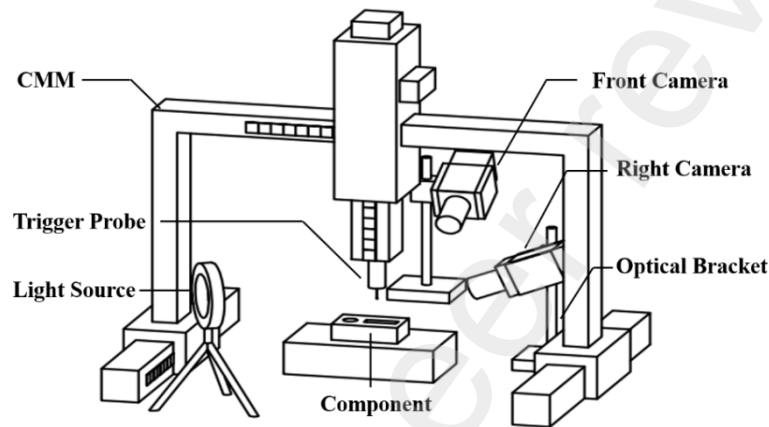


Fig. 1 General framework of the CMM intelligent measurement system

Figure 1 shows the general framework of the CMM intelligent measurement system [12]. The system mainly consists of a CMM with a trigger probe, two industrial cameras, light source, optical adjustment brackets, and intelligent measurement software. The trigger probe is used to acquire the coordinate points on the surface of the component. Two industrial cameras are mounted on the optical adjustment brackets, which are placed on the front and right side of the CMM to capture images of the component and the probe. The light source provides brightness to the system. Intelligent measurement software processes the information from the optical and mechanical sensors and guides the trigger probe to measure the component.

2.2 Workflow of the measurement system

The trigger probe and the component need to appear clearly in the camera field of view simultaneously before the measurement starts. Otherwise, the cameras' angle or the trigger probe position should be adjusted until the condition is met. The typical

features of the component are then intelligently measured using the intelligent measurement system with the workflow, as shown in Figure 2.

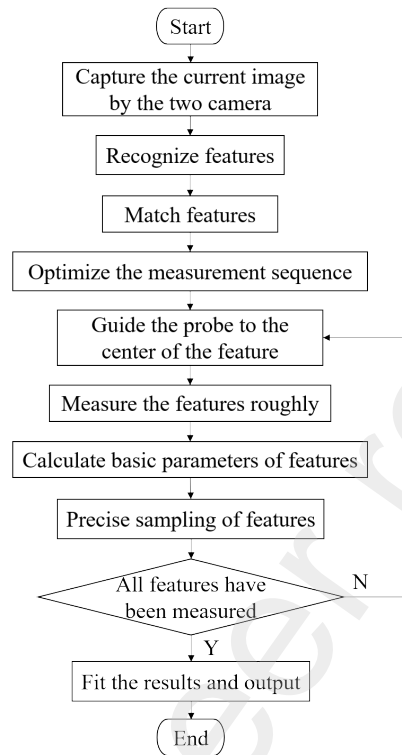


Fig. 2 Workflow diagram of the intelligent measurement system

3. Principles of the method

3.1 Feature detection

Realizing intelligent measurement first requires detecting the features to be measured from the images acquired using industrial cameras, that is, target detection. Target detection is divided into traditional target detection algorithms and deep learning-based target detection algorithms. Traditional algorithms have a large system resource overhead and require setting rules and various restriction parameters to ensure the performance of the algorithm. Moreover, the stability of the algorithm performance is poor. On the contrary, deep learning-based algorithms achieve autonomous learning through a data-driven approach and have better generalization capability. You Only Look Once (YOLO) is a single-stage deep learning target detection algorithm that can achieve good results in terms of detection accuracy and detection speed. This algorithm treats the target detection task as a regression problem of localization and classification, where the localization and classification probabilities of the target are obtained by an

end-to-end convolutional neural network with a direct prediction of the input image [13]. The YOLOv5 algorithm used in this study has the advantages of small model size, low deployment cost, good flexibility, and fast detection speed. Figure 3 shows the network model structure [14], which contains four main parts, namely, the input, backbone, neck, and head [15].

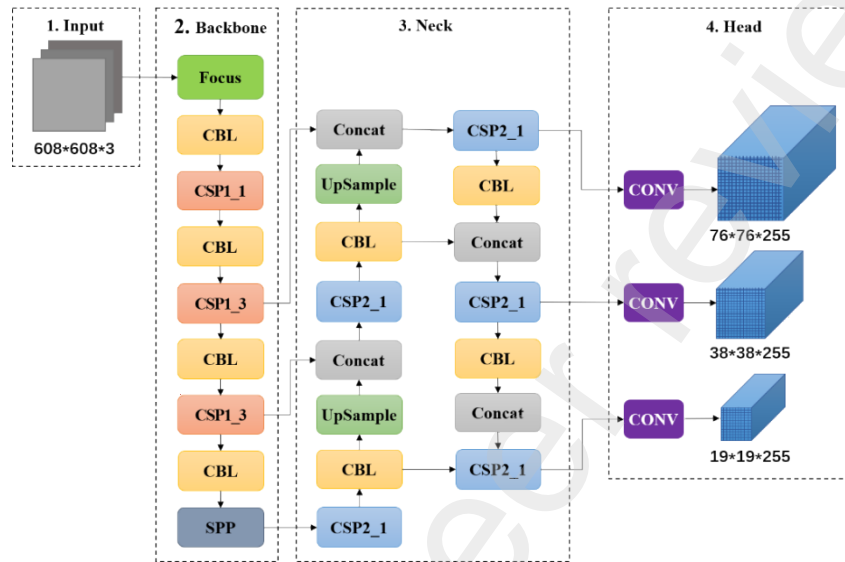


Fig. 3 Network structure of YOLOv5

To ensure that typical features on the component can be recognized accurately even under the circumstances of size/shape change, placement position change, local occlusion, surface material change, and others, the requirements for the typical feature dataset are as follows:

- (1) The number of images in the dataset should meet the number necessary for training, which is at least greater than 2000.
- (2) The pictures in the dataset include the component in different angles, different positions, and special cases with local occlusion.
- (3) The component samples have different surface textures and different types and numbers of typical feature distributions.
- (4) Labels and positioning frames of features are labeled using software.

In this study, 2050 photos of the component with typical features were taken using industrial cameras as the data set, including seven categories: *probe*, *hole*, *cylinder*, *slot*, *cslot*, *step*, and *ball*. *Probe* means probe, *hole* means hole, *cylinder* means cylinder,

slot means square slot, *cslot* means slot with circular arcs, *step* means square tab, and *ball* denotes ball. The data set is in the PASCAL VOC format, and the targets in the images are labeled using LabelImg.

Table 1. Hyperparameter setting of data enhancement

Method	Principle	Hyperparameter
mosaic	Crop four images randomly and then stitch them onto one image	0.8
fliplr	Random horizontal flip transformation of the image	0.4
flipud	Random vertical flip transformation of the image	0.2
hsv_h	Image color changes in hue	0.015
hsv_s	Image color changes in saturation	0.7
hsv_v	Image color changes in value	0.4
shear	Random affine transformation of the image	8.0
scale	Random scaling of the image	0.6

The data enhancement technique is used to increase the training data and enrich the training scenario for the measurement environment lighting changes and component size changes owing to the small number of available datasets. Table 1 shows the use of data enhancement methods and principles. The transformation coefficient of data enhancement is set to 10, and the augmented data set is a total of 20500 images. The data set is randomly divided into training and validation sets according to the ratio of 8:2, and the final number of images in the training set is 16400. Moreover, the number of images in the validation set is 4100. Model training produces one model every 800 times. The model with the highest mAP value among them is selected as the model with the best overall performance. Then, each hyperparameter of the model is adjusted to balance the accuracy and recall to find the optimal weight of the model that satisfies the feature detection accuracy. Tables 2 and 3 show the training configuration and hyperparameter settings.

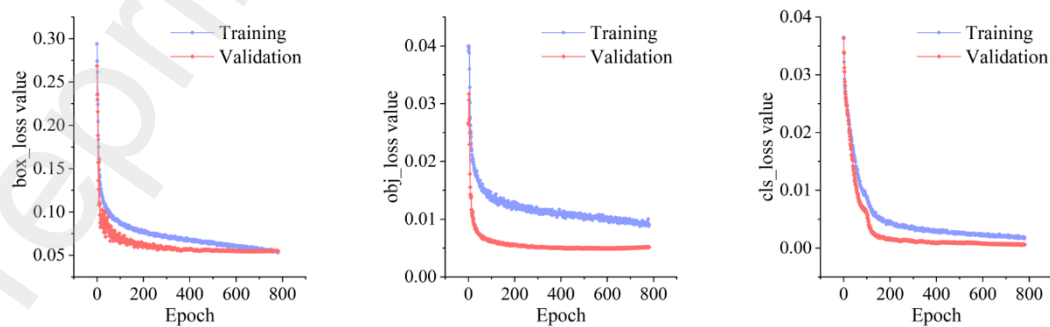
Table 2. Computational resource configuration for training

Name	Configuration
System	Windows10
CPU	Intel Core i7-12700
GPU	NVIDIA GeForce RTX 3080
Solid-State Drive	500GB
Python	Python3.6
CUDA	CUDA11.3
PyTorch	PyTorch1.7
OpenCV	OpenCV4.3.2

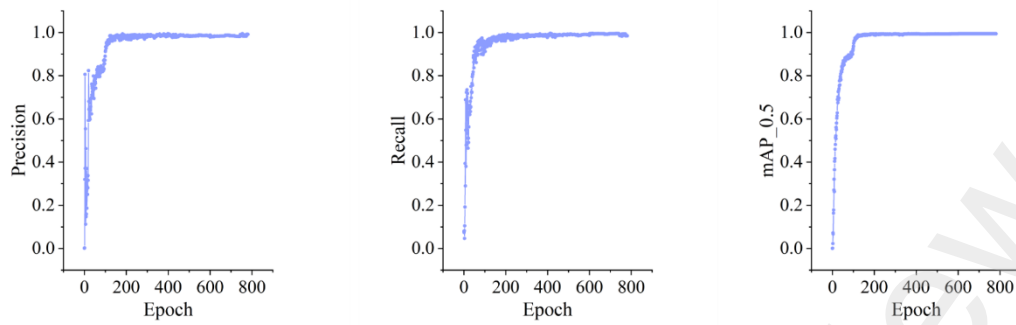
Table 3 Main training hyperparameter settings

Name	Meaning	Hyperparameter
Image size	Image size setting in training	800*800*3
Epochs	Maximum number of epochs per training	800
Batch size	Maximum batch size allowed by hardware	8
Optimizer	Types of optimizers	SGD
Momentum	Study rate momentum	0.937
lr0	Initialized learning rate	0.01
lrf	Learning rate coefficient	0.1
Warm up iteration	Warm-up learning epochs	3

Figure 4(a) shows the loss function curves of the training and validation sets. The losses of the bounding box regression, objective regression, and classification regression are reduced to the basic smoothness. Moreover, the loss of the validation set is observed, and no overfitting occurs. Figure 4(b) shows the fluctuation curves of the precision and recall of the validation set. The fluctuation of the curves is small, indicating that the training effect is good. Figure 5 depicts the PR curves for each category. The mAP of all classes is above 0.984, and the area of the PR curve for each category is close to 1, indicating that the model has a high detection rate.



(a) Loss function curves of the training and validation sets



(b) Fluctuation curves of precision, recall, and mAP of the validation set

Fig. 4 Loss variation and evaluation index of the training process

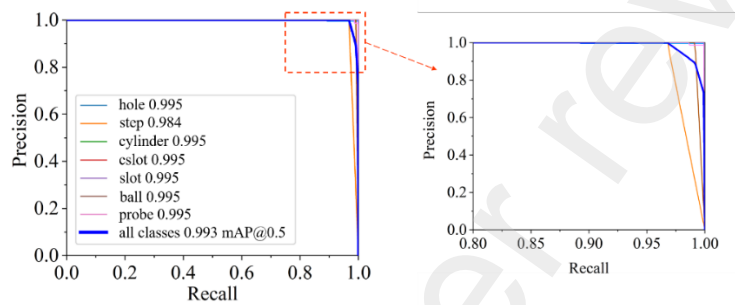


Fig. 5 PR curve

3.2 Feature matching

Detecting consistent key points in the captured component views is difficult because the two industrial cameras are positioned at 90° . Traditional image-matching algorithms, such as Scale Invariant Feature Transformation, Accelerated Robust Feature, and ORB, cannot complete the feature-matching work using these two images. The images captured using the camera do not reflect the true size and scale of the component owing to the perspective effect. Hence, the inverse perspective transformation can be used to remove the perspective effect in the images to generate the orthographic view of the workpiece. The two images are inverse perspective transformed separately to obtain the orthographic view of the component captured by the two cameras. The features in these two images must have a positional correspondence because of the uniqueness of the orthographic view of the component. The feature-matching algorithm in this study is designed based on the above principle.

3.2.1 Inverse perspective transformation model

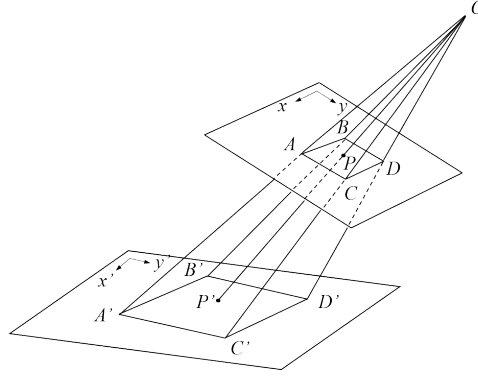


Fig. 6 Inverse perspective transformation geometric optical model

The inverse perspective transformation refers to the transformation that removes the perspective effect to produce an orthographic image of a 3D object in the plane. The four-point inverse perspective transformation method [16] solves the inverse perspective transformation matrix by correcting the correspondence between the front and back four points and substituting the coordinates. Figure 6 shows the geometric-optical model of the transformation. The camera's optical center is located at the O , and the projection of a point P on the imaging surface of the camera in the world coordinate system is P' . The coordinates of P in the world coordinate system after the inverse perspective transformation are inferred as follows:

$$\begin{bmatrix} X \\ Y \\ Z \end{bmatrix} = \begin{bmatrix} a_{11} & a_{12} & a_{13} \\ a_{21} & a_{22} & a_{23} \\ a_{31} & a_{32} & a_{33} \end{bmatrix} \begin{bmatrix} u_{p'} \\ v_{p'} \\ 1 \end{bmatrix}, \quad (1)$$

where $(u_{p'}, v_{p'})$ is the coordinates of P' in the pixel coordinate system. According to the scale invariance of the chi-square coordinates, we consider $[X, Y, Z]$ as the chi-square coordinates, let $a_{33}=1$, $X_{A''}=X/Z$, $Y_{A''}=Y/Z$, and get the following:

$$X_{A''} = \frac{a_{11}u_{p'} + a_{12}v_{p'} + a_{13}}{a_{31}u_{p'} + a_{32}v_{p'} + 1}, \quad (2)$$

$$Y_{A''} = \frac{a_{21}u_{p'} + a_{22}v_{p'} + a_{23}}{a_{31}u_{p'} + a_{32}v_{p'} + 1}. \quad (3)$$

The coordinates of $[X_{A''}, Y_{A''}]$ are the coordinates after the inverse perspective transformation. Four coordinate points in the original image and the corresponding coordinates of these four points in the new image are needed to select to solve the eight

unknowns from a_{11} to a_{32} in the Eqs. (2)–(3) to obtain the inverse perspective transformation matrix H .

$$H = \begin{bmatrix} a_{11} & a_{12} & a_{13} \\ a_{21} & a_{22} & a_{23} \\ a_{31} & a_{32} & a_{33} \end{bmatrix}. \quad (4)$$

3.2.2 Automatic target point detection

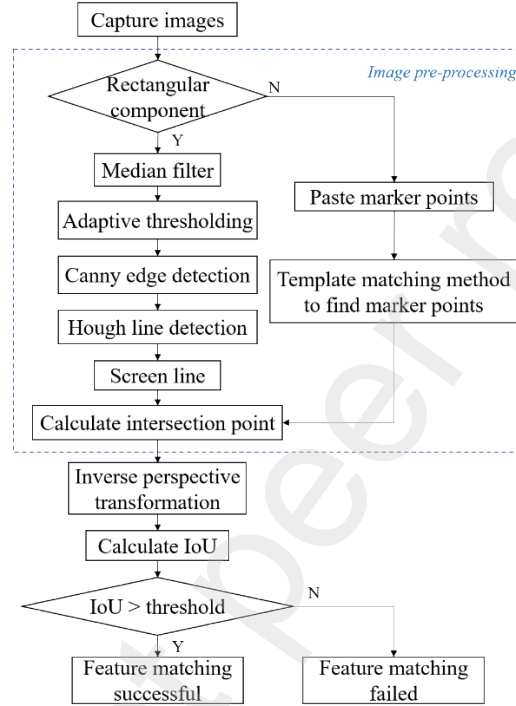


Fig. 7 Flow chart of automatic target point detection

Figure 7 shows the flow of the detection algorithm to obtain the four target points from the original image, and Figure 8 depicts the four target points $ABCD$ on the component. The outer contour of the components is divided into rectangular and non-rectangular. In a rectangular contour, the target point detection algorithm of rectangle is used. Otherwise, the target point detection algorithm for the non-rectangular shape is used.

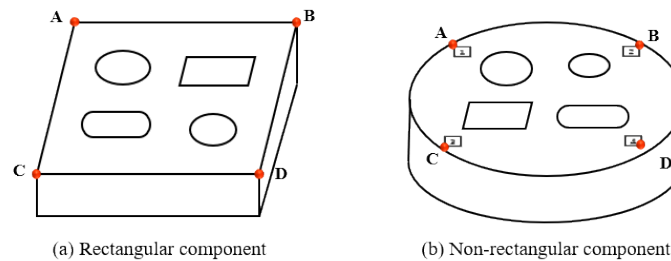


Fig. 8 Target point $ABCD$ position on the component

Image processing of rectangular components includes median filtering, adaptive thresholding, Canny edge detection, and Hough line detection. Considering that the image signal transmission and the decoding process will generate pretzel noise when disturbed, the use of median filtering can effectively remove the pretzel noise while better protecting the edge information in the image [17]. Binarization is used to distinguish the foreground and background areas to accurately obtain the edges of the component after removing the noise. The grayscale values of the foreground and background in each image are different because of the difference in the brightness of the ambient light source and the degree of reflected light from the workpiece surface. Adaptive thresholding can calculate local thresholds for different image regions based on their luminance distributions and can better distinguish between the component and background regions in the above case [18]. Canny edge detection [19] and Hough line detection [20] are then used to find straight lines in the image. The minimum enclosing rectangular box that can contain these features is calculated by the coordinates of the prediction box of each feature and the four straight lines of suitable length that are closest to the four directions of the top, bottom, left, and right of the minimum enclosing rectangular box. Moreover, the intersection point of these four straight lines is the target point $ABCD$.

For non-rectangular contours, square labels need to be applied to the surface of the measured component in advance. Two conditions need to be ensured when applying the labels: (1) the four labels are at the four vertices of a rectangular area, and (2) the rectangular area can contain all the target features that need to be measured. A label database is created for the template matching algorithm to identify labels. The template matching of the correlation coefficient method [21] identifies square labels by calculating the correlation coefficient between the template and the image region. If the maximum value of the correlation coefficient is greater than the threshold value, the template matching is considered successful, and its target area location is confirmed. This method can achieve satisfactory target matching under various conditions, such as translation of the target, $\pm 180^\circ$ rotation, and $\pm 50\%$ zoom change, which can improve the success rate and stability of template matching. Then, the identified tag regions are

set as the region of interest, and four corner points on the tags are extracted using Harris corner point detection [22]. The top-left, top-right, bottom-left, and bottom-right vertices of the four labels are then selected as the four points $ABCD$ for the calculation of the inverse perspective transformation matrix, respectively.

3.2.3 Matching algorithm

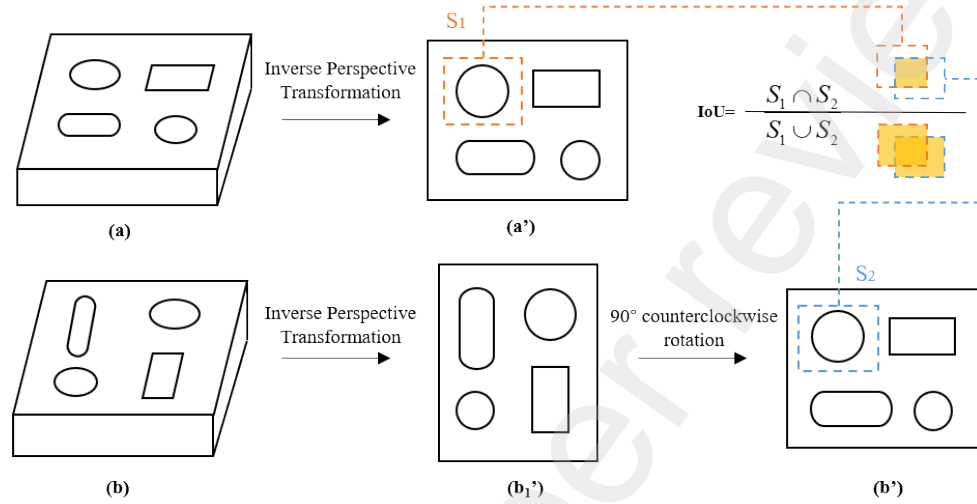


Fig. 9 Schematic diagram of feature matching based on inverse perspective transformation

As shown in Figure 9, image a taken by the front side camera A is converted to image a' after inverse perspective transformation, and image a' is the orthographic projection of the component taken by the front side camera A . The image b taken by the right camera B is converted to image b_1' after inverse perspective transformation. Then, image b_1' is rotated 90° counterclockwise to obtain image b' , and image b' is the orthographic image of the component taken by the right camera B . Taking one of the hole features in the component as an example, the feature detection will obtain the label of each feature in images a and b and the coordinate value of the prediction frame. Moreover, the coordinate value of the prediction frame in images a' and b' will be calculated according to the inverse perspective transformation matrix H . If more than one prediction frame overlaps with S_1 , the prediction frames with different labels are excluded first, and then, the intersection ratio IoU between S_1 and S_2 is calculated according to the formula in Figure 9. In addition, the prediction frame with the maximum value of IoU is selected as the feature to be matched. When the result of this calculation is greater than the threshold value $Thre$, the feature corresponding to S_1 in

image a' is considered successfully matched with the feature corresponding to S_2 in image b' . After the features are matched, the probe features are matched as each image has only one probe. The probes identified in the two images are directly matched together.

3.3 Route planning and sampling strategy

The basic parameters of the feature need to be measured first to calculate the exact sampling points after the probe is guided above the center of the feature. Only a few points on the surface of the feature are needed to calculate the basic parameters of the feature, regarded as a rough measurement of the feature. After the rough measurement is finished, the basic dimensional information of the feature is obtained, and the exact sampling point distribution strategy of the feature is designed. The coordinates of the sampling points are calculated based on this basic dimensional information to drive the probe to measure the feature along the three-axis motion of the CMM.

The typical features are divided into two categories, which are rotating and non-rotating body features. A rotating body feature is a geometric feature enclosed by a closed rotating surface, such as holes, cylinders, or balls. Non-rotating body features are features other than rotating body features, such as square slots, round slots, and steps.

3.3.1 Rough measurement path planning

3.3.1.1 Rough measurement path planning for rotating body features

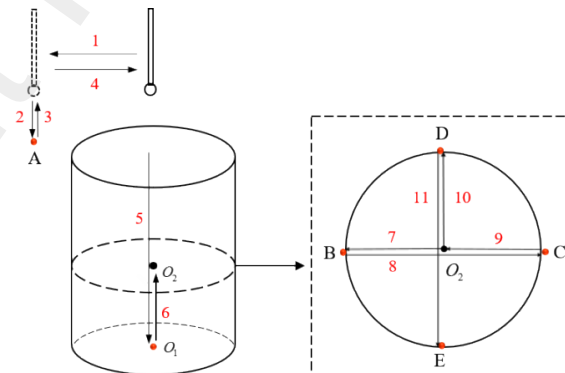


Fig. 10 Rough measurement path of the hole

Figure 10 shows the rough measurement path of the hole. A point A on the plane where the hole is located is first measured along paths 1–2 after the probe is guided

above the center of the hole, where the distance x moved by path 1 is calculated from the information in the image as follows:

$$x = K \times (u_{feature0} - u_{o-tip}), \quad (5)$$

where K is the scale factor between the actual distance in the world coordinate system and the pixel in the pixel coordinate system, $u_{feature0}$ is the coordinate of the lower left corner of the feature detection frame in the u axis direction, and u_{o-tip} is the coordinate value of the probe center in the u axis direction.

Then, the hole returns to the initial center position along paths 3–4. The probe sinks until it touches the bottom of the hole to obtain the coordinate point O_1 , then ascend a distance to O_2 , and measure the four points $BCDE$ on the cross-section of O_2 along paths 7–11. The depth h_{hole} is calculated from the distance between A and O_1 on the z -axis, and the diameter d_{hole} of the hole is obtained by fitting the four points $BCDE$.

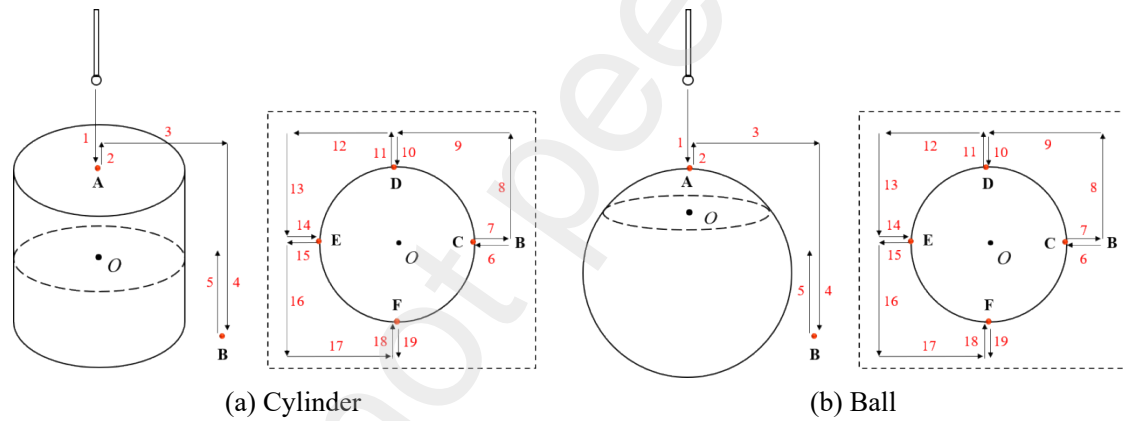


Fig. 11 Rough measurement path of the cylinder and ball

Figure 11(a) shows the rough measurement path of the cylinder. The probe first sinks to measure point A on the upper surface of the cylinder after the probe is guided above the center of the cylinder. Then, point B on the surface where the bottom surface of the cylinder is located is measured along paths 2–4, where distance x moved by path 3 is calculated by Eq. (5). Then, the probe rises, and the four points $CDEF$ on the circular section of the cylinder at the height of the current probe are measured, whose paths are 6–19. The distance calculation for paths 8, 9, 12, 13, 16, and 17 is the same as the distance calculation for path 3. The height of the cylinder $h_{cylinder}$ is calculated by the distance between A and B on the Z -axis, and the diameter of the cylinder $d_{cylinder}$ is

obtained by fitting the four points of $CDEF$. Figure 11(b) shows the rough measurement path of the ball, and its rough measurement path is similar to that of the cylinder.

3.3.1.2 Rough measurement path planning for non-rotating body features

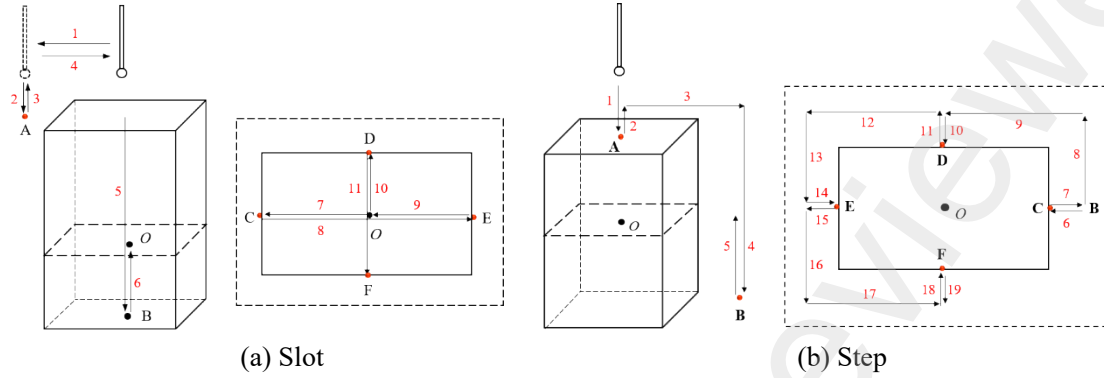


Fig. 12 Rough measurement path of the slot and step

Figure 12(a) depicts the rough measurement path of the slot. The overall path is the same as the coarse measurement path of the hole. The depth h of the slot is calculated from the distance between A and B on the Z -axis, and the length l of the slot is as follows:

$$l = l_{CE} \cdot \cos \theta, \quad (6)$$

where l_{CE} is the distance between the two points of CE in the X -axis direction and θ is the tilt angle of the square slot with respect to the X -axis of the CMM, which is obtained through image processing. Similarly, the width w of the square slot is as follows:

$$w = l_{DF} \cdot \cos \theta, \quad (7)$$

where l_{DF} is the distance between the two points of DF in the direction of the Y -axis.

Figure 12(b) shows the rough measurement path of the step. Its overall path is the same as the rough measurement path of the cylinder. The height h , the length l , and the width w of the step are the same as the slot.

3.3.2 Precise distribution of sampling points

3.3.2.1 Precise distribution of sampling points for rotating body features

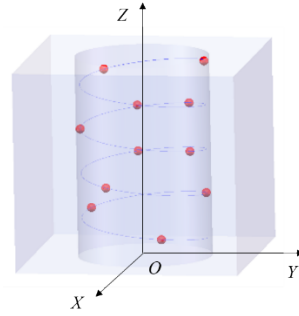


Fig. 13 Distribution of sampling points for column

Figure 13 shows the distribution of sampling points for the accurate measurement of the column surface, and its sampling point distribution law follows the phyllodes distribution model. This model uses the distribution law of leaves on plant rhizomes to ensure a uniform staggered distribution of sampling points on the column surface [23]. The number of sampling points is set to n . The height h and diameter d of the column surface are calculated through rough measurement, and the coordinate value of the i th sampling point in the coordinate system of CMM can be calculated by the phyllodes distribution model [24]:

$$\begin{cases} x_i = \frac{d}{2} \cdot \cos \theta_i \\ y_i = \frac{d}{2} \cdot \sin \theta_i, \\ z_i = h \cdot \frac{i}{n} \end{cases} \quad (8)$$

where θ_i is the angle between the line of the i th sampling point and the point O and the X axis, which is calculated by Eq. (9).

$$\theta_i = 137.508^\circ \cdot i \quad (9)$$

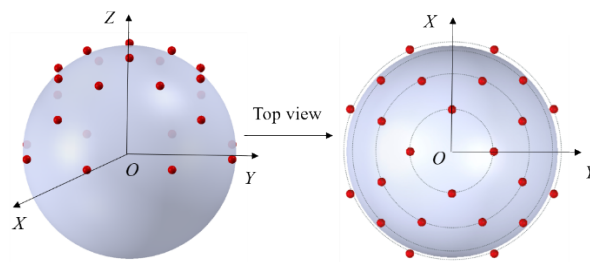


Fig. 14 Distribution of sampling points for the ball

Figure 14 shows the exact sampling point distribution of the ball. The sampling points on the ball should be distributed on its surface as evenly as possible. The height h of the exposed plane of the ball and the diameter d are obtained after rough measurement. If $h > d/2$, then only the upper half of the ball is measured, and let $h = d/2$. The upper half of the ball is divided into four equal layers according to its circularity angle θ . The corresponding circularity angle α_i of the i th layer is as follows:

$$\begin{cases} \theta = \arccos \frac{d-2h}{d} \\ \alpha_i = \frac{\theta}{4} \cdot i \end{cases} \quad (10)$$

The sampling points of two adjacent layers are staggered, which can ensure the uniform distribution of sampling points on the sphere. The coordinates of each sampling point are calculated as follows:

$$\begin{cases} x_i = \frac{d}{2} \cdot \sin \alpha_i \cdot \cos \beta_j \\ y_i = \frac{d}{2} \cdot \sin \alpha_i \cdot \sin \beta_j \\ z_i = \frac{d}{2} \cdot \cos \alpha_i \\ \beta_j = \frac{2\pi j}{n} \end{cases}, \quad (11)$$

where i is the number of layers where the point is located, j is the j th sampling point of the sampling point of the i th layer, α_i is the corresponding circular angle in layer i , β_j is the angle between the j th point in layer i and the coordinate axis in the positive X direction, and n is the number of sampling points of a layer.

3.3.2.2 Precise distribution of sampling points for non-rotating body features

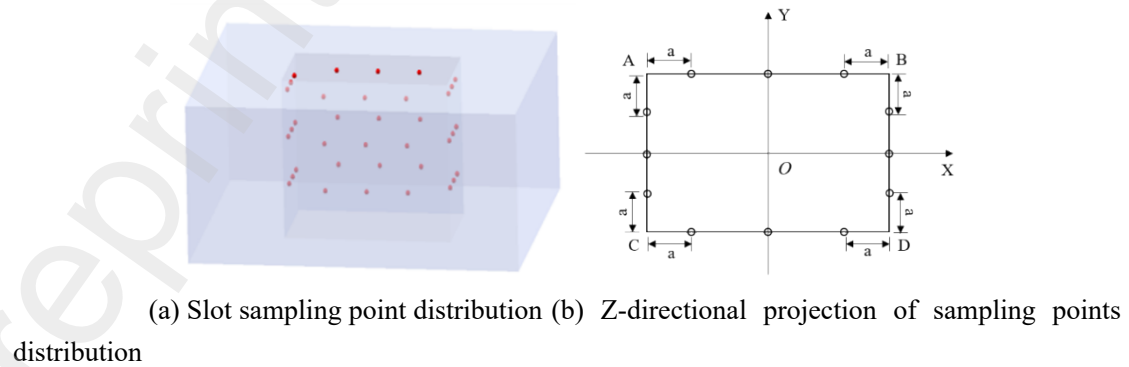
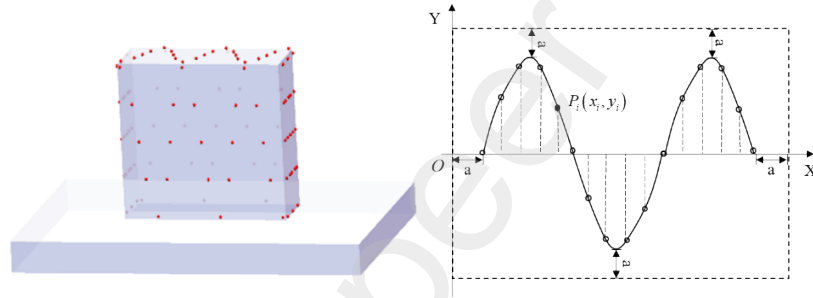


Fig. 15 Distribution of sampling points for the slot

Figure 15 shows the distribution of slot sampling points, and the sampling strategy of uniform distribution is adopted. From the rough measurement results, the depth h ,

the length l , and the width w of the slot can be calculated. The number of measurement layers m of the slot and the number of measurement points n per layer are set, the measurement points are distributed evenly to each face, and the points are laid at equal distances on the face. The distance between the edge measurement point of each face and the edge of the face is set as a . The coordinates of the i th sampling point in the j th layer on the AB face are calculated by Eq. (12). The coordinates of the sampling points of other planes are calculated in the same way.

$$\begin{cases} x_i = -\frac{l}{2} + a + \frac{4l-8a}{n} \cdot i \\ y_i = \frac{w}{2} \\ z_i = a + \frac{h-2a}{m} \cdot j \end{cases} \quad (12)$$



(a) Step sampling point distribution (b) Z-directional projection of sampling point distribution

Fig. 16 Distribution of sampling points for step

Figure 16(a) shows the distribution of sampling points on the step. Using the S-shaped path to place points equally spaced on the five planes of the bump ensures the uniformity of the sampling point distribution but also makes the sampling points on each layer interleaved with each other, which can better reflect the error situation on the planes. The sampling points on each plane are distributed on a trigonometric curve, as shown in Figure 16(b). The coordinates of the points can be calculated based on the height h , the length l , and the width w of the step, and Eq. (13) is the coordinates of the sampling points on the upper surface. n is the number of sampling points on the plane, and a is the distance between the edge measurement point and the edge of the face. The coordinates of the sampling points on the other surfaces of the step are calculated in the same way.

$$\begin{cases} x_i = \frac{l}{n} \cdot i \\ y_i = \left(\frac{w}{2} - a \right) \sin \left(\frac{5\pi}{l-2a} x_i \right) \\ z_i = h \end{cases} \quad (13)$$

4. Experiments and results

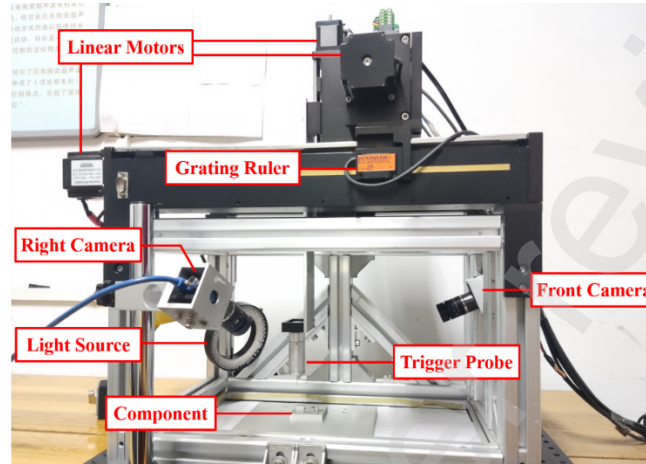


Fig. 17 Physical diagram of the CMM intelligent measurement system

Figure 17 shows the physical diagram of the CMM intelligent measurement system. The system is equipped on a homemade CMM, which is equipped with a linear motor (57BYGH250B) and a raster scale (Renishaw RH100×30.05 A) in each direction with a resolution of 1 μm . The linear motor is controlled by a pulse signal from a motion control card (LeadShine DMC3000) and driven by a driver (LeadShine DM542). A home-made industrial probe with a trigger repeatability of 0.5 μm and a resolution of 0.5 μm is mounted on the Z-axis of CMM, and a probe tip on the probe is a 1mm diameter ruby ball Renishaw probe tip. The trigger signal generated by the probe is recorded by an acquisition card (NI PCI-6259) and transmitted to the PC. Two lenses (Computer M1224-MPW2) are used for the selected industrial camera (MER-301-125U3M): on the front and right side of the CMM, respectively. The camera image resolution is 2048*1536, and the pixel size is 3.45 μm *3.45 μm . The ring light source (LED-A5067) is placed on the left rear side of the CMM to provide brightness for the whole system.

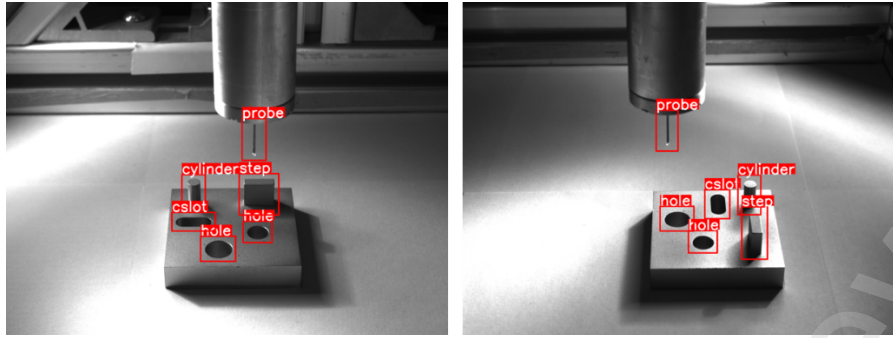


Fig. 18 Detection results of images *a*, *b*

The experiment uses an object with *step*, *cylinder*, *hole*, and *cslot* features as the component to be measured. First, the component's position is adjusted, and the probe is moved so that the component and the probe are clearly presented in the camera field of view simultaneously. The front-side camera *A* and the right-side camera *B* take the current images *a* and *b*, which are input into the trained feature detection model. Figure 18 shows the detection results. Table 4 presents the feature labels and the coordinate values of their detection frames under the image coordinate system.

Table 4 Feature labels and coordinate values of detection frames

Image	Label	No.	Confidence	Coordinate values of detection frame/pixel			
				A	B	C	D
Image <i>a</i>	<i>probe</i>	0	0.85	(1093,537)	(1205,537)	(1093,731)	(1205,731)
	<i>step</i>	1	0.95	(1080,791)	(1264,791)	(1080,983)	(1264,983)
	<i>cylinder</i>	2	0.95	(814,796)	(924,796)	(814,959)	(924,959)
	<i>cslot</i>	3	0.92	(768,970)	(970,970)	(768,1057)	(970,1057)
	<i>hole</i>	4	0.96	(1098,1011)	(1233,1011)	(1098,1110)	(1233,1110)
	<i>hole</i>	5	0.94	(901,1080)	(1064,1080)	(901,1197)	(1064,1197)
Image <i>b</i>	<i>hole</i>	0	0.96	(1047,1054)	(1182,1054)	(1047,1158)	(1182,1158)
	<i>hole</i>	1	0.94	(916,942)	(1074,942)	(916,1057)	(1074,1057)
	<i>cslot</i>	2	0.92	(1123,865)	(1240,865)	(1123,1000)	(1240,1000)
	<i>cylinder</i>	3	0.92	(1277,798)	(1384,798)	(1277,982)	(1384,982)
	<i>step</i>	4	0.90	(1295,944)	(1415,944)	(1295,1187)	(1415,1187)
	<i>probe</i>	5	0.84	(898,499)	(1000,499)	(898,688)	(1000,688)

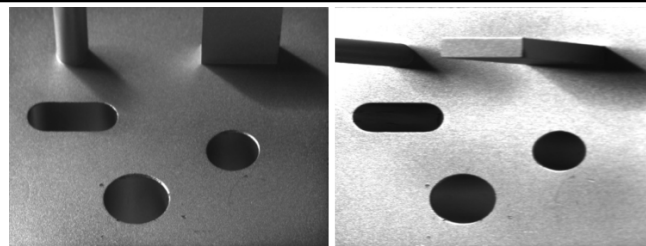


Fig. 19 Images of inverse perspective transformation result

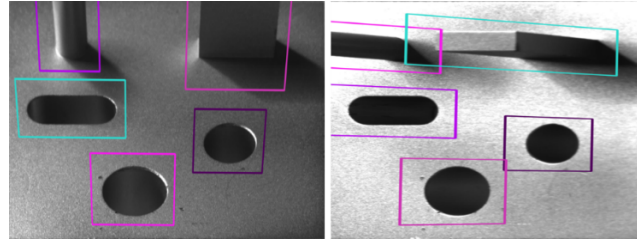


Fig. 20 Schematic diagram of prediction frame after coordinates conversion

The inverse perspective transformation matrix of image a is:

$$H_a = \begin{pmatrix} 5.7653 & 0.5300 & -4879.3187 \\ 0.0819 & 7.5790 & -6603.5477 \\ 0.0176 & 0.0006 & 1 \end{pmatrix}, \text{ the transformation matrix of image } b \text{ is:}$$

$$H_b = \begin{pmatrix} 0.1162 & 10.5324 & -9297.7151 \\ -4.4894 & 0.8323 & 5698.1876 \\ 0.0093 & 0.0007 & 1 \end{pmatrix}, \text{ and Figure 19 shows the transformation results. The}$$

coordinates of the transformed prediction frame are calculated according to the matrix H and the prediction frame coordinates in Table 4. The new image boundary is used as the prediction frame boundary when the prediction frame is transformed beyond the set image size. Figure 20 shows the schematic diagram. The prediction frame with the same feature label and the largest overlapping area is found according to the screening principle mentioned in the feature matching algorithm. IoU is calculated, and the IoU threshold is set to 0.3. Table 5 shows the matching result.

Table 5 Feature matching result

Image a		Image b		Area of overlap /(pixel*pixel)	IoU	Result of feature matching
No.	Label	No.	Label			
0	<i>probe</i>	5	<i>probe</i>	-	-	Success
1	<i>step</i>	4	<i>step</i>	199409.6869	0.3354	Success
2	<i>cylinder</i>	3	<i>cylinder</i>	114523.2569	0.4166	Success
3	<i>cslot</i>	2	<i>cslot</i>	223719.7623	0.7560	Success
4	<i>hole</i>	0	<i>hole</i>	191612.4563	0.8352	Success
5	<i>hole</i>	1	<i>hole</i>	225385.8926	0.7328	Success

The key to the intelligent method is the accuracy of detection and matching results. If each feature on the component can be accurately detected and matched, then the feature measurement can later be completed successfully. A test set is made by changing the factors that may affect the success rate of the algorithm, such as component placement, component type, light source brightness, and camera shooting angle, to verify the success rate of the detection and matching algorithms. The number

of samples in this test set is 250, as shown in Figure 21. The test set images were input into the algorithm for detection and matching, and Table 6 presents the success rate of its results.

From Table 6, the degree of occlusion of features has a large impact on the results of feature matching. A hole is used as the object to verify the effect of the obscured proportion on the success rate of feature matching, and the probe position is moved in the front-side camera field of view so that it produces different degrees of obscuration of the hole in the field of view. The ratio of the occlusion area to the area of the hole is 10%–100%, increasing by 5% in sequence. Moreover, both cameras take pictures and perform feature matching. The IoU threshold is changed to verify its effect on the matching results. The experimental results show that when the percentage of feature unobstructed area is greater than the IoU threshold, it can be matched successfully. Therefore, individual features in the cameras' field of view should be kept unobstructed as much as possible during measurement.

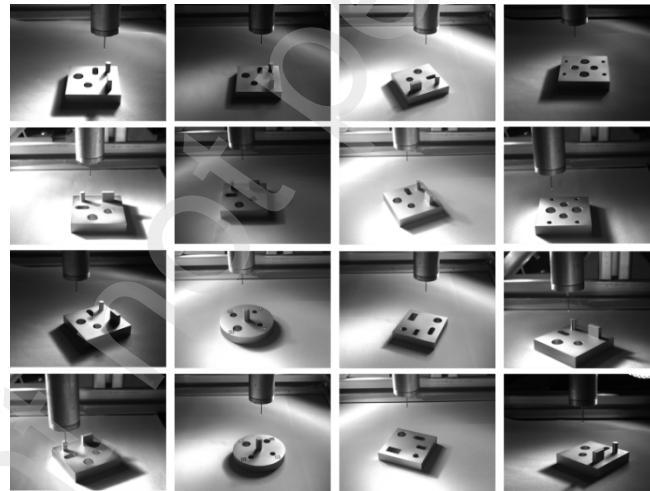


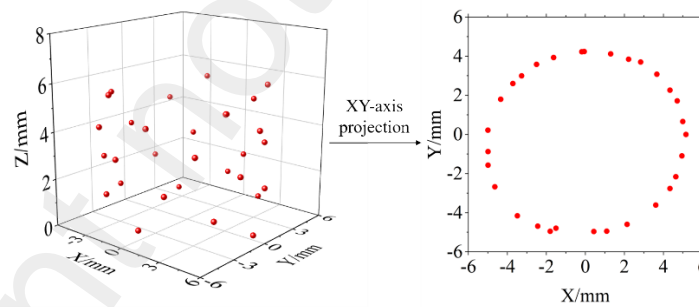
Fig. 21 Detection and matching test set samples

Table 6 Success rate of the detection and matching results

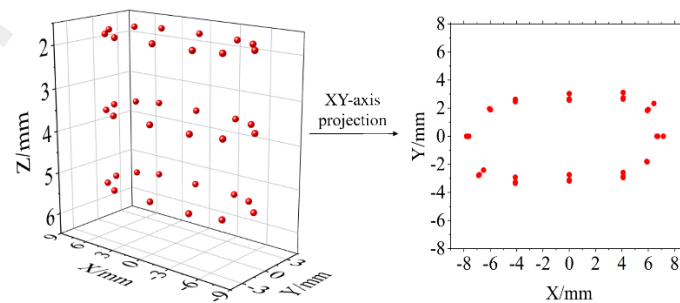
Influencing factors	Number of images	Detection success rate	Matching success rate
Component placement	50	100%	100%
Component type	50	100%	100%
Light source brightness	50	100%	100%
Camera shooting angle	50	100%	100%
Degree of feature occlusion	50	100%	92%

The coordinates (x, y) of each feature center in the coordinate system xOy are obtained from the relative pixel differences between the probe tip and each feature center in images a and b . The whole measurement process is considered a TSP for the probe tip, and the ant colony algorithm is used to plan the optimal measurement order of the features. The initialization algorithm parameters are set as follows: the number of ants is 30, the importance of the pheromone in the ant selection path is $\alpha = 2$, the importance of the heuristic factor in the ant selection path is $\beta = 5$, the concentration of pheromone at the initial moment is $\tau = 0.1$, and the maximum number of iterations is set to 500. The optimal detection order is calculated as 5–3–2–1–4 based on the feature label serial number identified in the right camera image.

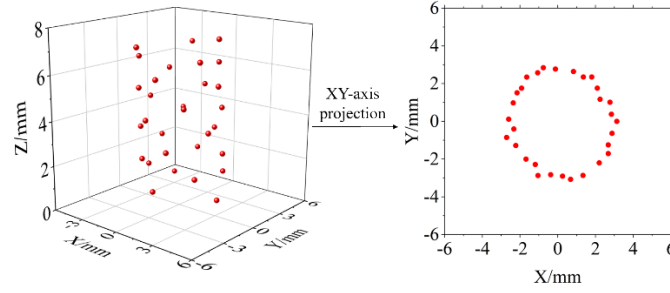
The guidance algorithm is used to guide the probe tip closer to the feature centers in the order of measurement. The features are measured roughly first, and the obtained information is used to calculate the coordinate points for an exact sampling and then to measure the feature again. Figure 22 shows the feature's exact sampling point map. Then, the basic parameters of the feature, such as the diameter of the hole, the diameter of the cylinder, and the length and width of the slot, can be obtained by fitting the coordinates of the sampling points.



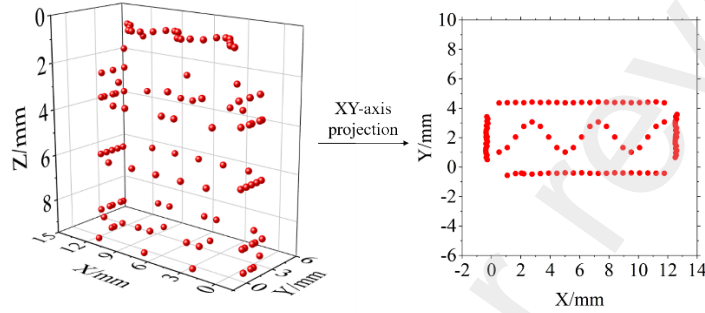
(a) Measurement results of *hole₁*



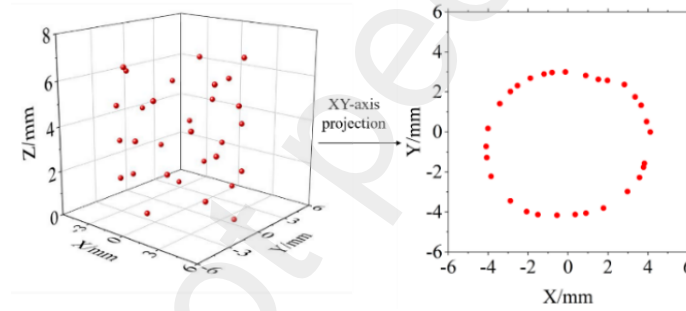
(b) Measurement results of *cs1ot*



(c) Measurement results of *cylinder*



(d) Measurement results of *step*



(e) Measurement results of *hole₂*

Fig. 22 Feature exact sampling point map

5. Conclusion

This study proposed an intelligent measurement method and system for CMM to automatically measure typical features. Experiments on intelligent measurement of a component with multiple typical features verify the correctness and effectiveness of the proposed method and system. The measurement can be completed 100% when the features are unobstructed in the camera field of view. Moreover, the accuracy of the measurement can be guaranteed when the percentage of feature unobstructed area is larger than the matching IoU threshold when occlusion occurs. This method does not require CAD and has the advantages of intelligence, high efficiency, and low cost. The system has good universality and can be installed on various types of CMMs. In future

research, deep learning algorithms will be used to develop more intelligent measurements of composite types of features.

6. Reference

- [1] Nasr E, Kamrani A K. A new methodology for extracting manufacturing features from CAD system[J]. Computers & Industrial Engineering, 2006, 51(3):389-415.
- [2] Le T, Ye D. A primitive-based 3D segmentation algorithm for mechanical CAD models[J]. Computer Aided Geometric Design, 2017, 52–53:231-246.
- [3] Hase V J, Bhalerao Y J, Verma S, et al. Blend recognition from CAD mesh models using pattern matching[C]. 1st International Conference on Advances in Mechanical Engineering and Nanotechnology (ICAMEN), 2019, 2148:030029.
- [4] Cho M W, Lee H, Yoon G S, et al. A feature-based inspection planning system for coordinate measuring machines[J]. The International Journal of Advanced Manufacturing Technology, 2005(9/10):26.
- [5] Durrant-Whyte H F. Sensor Models and Multisensor Integration[J]. International Journal of Robotics Research, 1988, 7(6):97-113.
- [6] Bradley C, Chan V. A Complementary Sensor Approach to Reverse Engineering[J]. Journal of Manufacturing Science & Engineering, 2001, 123(1):74-82.
- [7] Zhao H, Kruth J P, Gestel N V, et al. Automated dimensional inspection planning using the combination of laser scanner and tactile probe[J]. Measurement, 2012, 45(5):1057–1066.
- [8] Yunbao Huang, Xiaoping. A Dynamic Sensing-and-Modeling Approach to Three-Dimensional Point- and Area-Sensor Integration[J]. Journal of manufacturing science and engineering, 2007, 129(3):623-635.
- [9] Yu Z, Wang T, Wang P, et al. Rapid and Precise Reverse Engineering of Complex Geometry Through Multi-Sensor Data Fusion[J]. IEEE Access, 2019, 7:165793-165813.
- [10] Lu K, Wang W. A multi-sensor approach for rapid and precise digitization of free-form surface in reverse engineering[J]. The International Journal of Advanced Manufacturing Technology, 2015, 79(9-12):1983-1994.

- [11] Z.Y. Cheng, Luan He, Yuan Sun, et al. New method and system of automatically moving a CMM probe tip into holes with submillimeter diameter and high aspect ratio[J]. Instrum. , 2021, 16(6): 06042.
- [12] Z. Y. Cheng, Y. Sun, H. Luan, H. -L. Li, Q. -S. Pan and R. J. Li. Self-Calibration Vision Method and System for Automatically Moving CMM Stylus into Micro Holes. IEEE Sensors Journal, 2022, 22(4): 3579-3584.
- [13] Redmon J, Divvala S, Girshick R, et al. You only look once: Unified, real-time object detection[C]. Proceedings of the IEEE conference on computer vision and pattern recognition. 2016, 779-788.
- [14] Jocher, G., Stoken, A., Borovec, J. Ultralytic/Yolov5. Available online: <https://github.com/-ultralytics/yolov5> (accessed on 25 June 2021).
- [15] Jing Y, Ren Y, Liu Y, Wang D, Yu L. Automatic Extraction of Damaged Houses by Earthquake Based on Improved YOLOv5: A Case Study in Yangbi[J]. Remote Sens. 2022, 14(2):382.
- [16] A. Sun, Y. Wei, Y. Zhou, J. Wang and Y. Liu, 3D Estimation of Single Image based on Homography Transformation[C]. 2022 IEEE 6th Information Technology and Mechatronics Engineering Conference (ITOEC), Chongqing, China, 2022, 727-732.
- [17] George G, Oommen R M, Shelly S, et al. A Survey on Various Median Filtering Techniques for Removal of Impulse Noise from Digital Image[C]. 2018 Conference on Emerging Devices and Smart Systems (ICEDSS). IEEE, 2018.
- [18] Chan F, Lam F K. Adaptive thresholding by variational method[J]. IEEE Trans Image Process, 1998, 7(3):468-473.
- [19] C. Wu et al. An Improved Canny Edge Detection Algorithm with Iteration Gradient Filter[C]. 2022 6th International Conference on Imaging, Signal Processing and Communications (ICISPC), Kumamoto, Japan, 2022, 16-21.
- [20] Ye H, Shang G, Wang L, et al. A new method based on hough transform for quick line and circle detection[C]. 2015 8th International Conference on Biomedical Engineering and Informatics (BMEI). IEEE, 2015, 52-56.

- [21] Y. Konishi, Y. Kotake, Y. Ijiri, and M. Kawade. Fast and precise template matching based on oriented gradients[C]. in Proc. Int. Conf. Comput. Vis., 2012, 7585:607-610.
- [22] Han S, Yu W, Yang H, et al. An Improved Corner Detection Algorithm Based on Harris[C]. 2018 Chinese Automation Congress (CAC), 2018, 1575-1580.
- [23] Chen B. Optimum and arrangement technology of abrasive topography for brazed diamond grinding disc[J]. International Journal of Refractory Metals & Hard Materials, 2021, 95(1):105455.
- [24] Yeatts F R. A growth-controlled model of the shape of a sunflower head[J]. Mathematical Biosciences, 2004, 187(2):205-221.